

# Small, Smart, and LDLR-Specific Micelles Augment Sorafenib Therapy of Glioblastoma

Jingjing Wei, Yifeng Xia, Fenghua Meng,\* Dawei Ni, Xinyun Qiu, and Zhiyuan Zhong\*



Cite This: *Biomacromolecules* 2021, 22, 4814–4822



Read Online

ACCESS |



Metrics & More

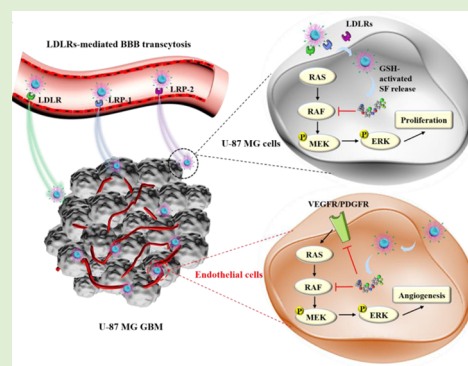


Article Recommendations



Supporting Information

**ABSTRACT:** Targeted molecular therapy, for example, with sorafenib (SF) is considered as a new and potent strategy for glioblastoma (GBM) that remains hard to treat today. Several clinical trials with SF, as monotherapy or combination therapy with current treatments, have not met the clinical endpoints, likely as a result of the blood–brain barrier (BBB) and inferior GBM delivery. Here, we designed and explored small, smart, and LDLR-specific micelles to load SF (LDLR-mSF) and to improve SF therapy of GBM by enhancing BBB penetration, GBM accumulation, and cell uptake. LDLR-mSF with 2.5% ApoE peptide functionality based on poly(ethylene glycol)-poly( $\epsilon$ -caprolactone-*co*-dithiolane trimethylene carbonate)-mefenamate exhibited nearly quantitative SF loading, small size (24 nm), high colloidal stability, and glutathione-activated SF release. The *in vitro* and *in vivo* studies certified that LDLR-mSF greatly enhanced BBB permeability and U-87 MG cell uptake and caused 10.6- and 12.9-fold stronger anti-GBM activity and 6.0- and 2.5-fold higher GBM accumulation compared with free SF and non-LDLR mSF controls, respectively. The treatment of an orthotopic human GBM tumor model revealed that LDLR-mSF at a safe dosage of 15 mg of SF/kg significantly retarded tumor progression and improved the survival rate by inducing tumor cell apoptosis and inhibiting tumor angiogenesis. These small, smart, and LDLR-specific micelles provide a potential solution to enhance targeted molecular therapy of GBM.



## INTRODUCTION

Glioblastoma (GBM) remains a hard-to-treat malignancy today.<sup>1–3</sup> Dysregulation of the tyrosine kinase signaling pathway is closely related to tumor development, and thus, tyrosine kinase inhibition is an important strategy for potential anticancer therapy. Based on the molecular alterations in signaling pathways in GBM such as RAS-RAF-mitogen-activated protein kinase (RAS/RAF/MAPK),<sup>4,5</sup> phosphatidylinositol-3 kinase-Akt-mammalian target of rapamycin (PI3K/Akt/mTOR),<sup>6,7</sup> and polo-like kinases (PLK1),<sup>8</sup> kinase inhibitors such as sorafenib (SF),<sup>9</sup> voxalisib (XL765),<sup>10</sup> and BI 2536<sup>11</sup> are under preclinical and clinical development. In particular, SF therapy is considered as a new and potent strategy in that it could not only effectively inhibit cancer cell proliferation and prevent angiogenesis by blocking the RAF-MEK-ERK (MAPK) pathway, vascular endothelial growth factor receptor (VEGFR), and platelet-derived growth factor receptor (PDGFR) but also selectively deplete human GBM tumor-initiating cells (GICs).<sup>12</sup> SF has been approved for clinical therapy of hepatocellular carcinoma, advanced renal cell carcinoma, and differentiated thyroid cancer and also shows clinical benefits for lung cancer, breast cancer, and melanoma.<sup>13,14</sup> Several clinical trials with SF, as monotherapy or combination therapy with current treatments, for example, bevacizumab,<sup>15</sup> erlotinib,<sup>16</sup> and tipifarnib,<sup>9</sup> for treating GBM failed to meet the clinical endpoints, likely as a result of the blood–brain barrier (BBB) and inferior GBM delivery.<sup>17,18</sup>

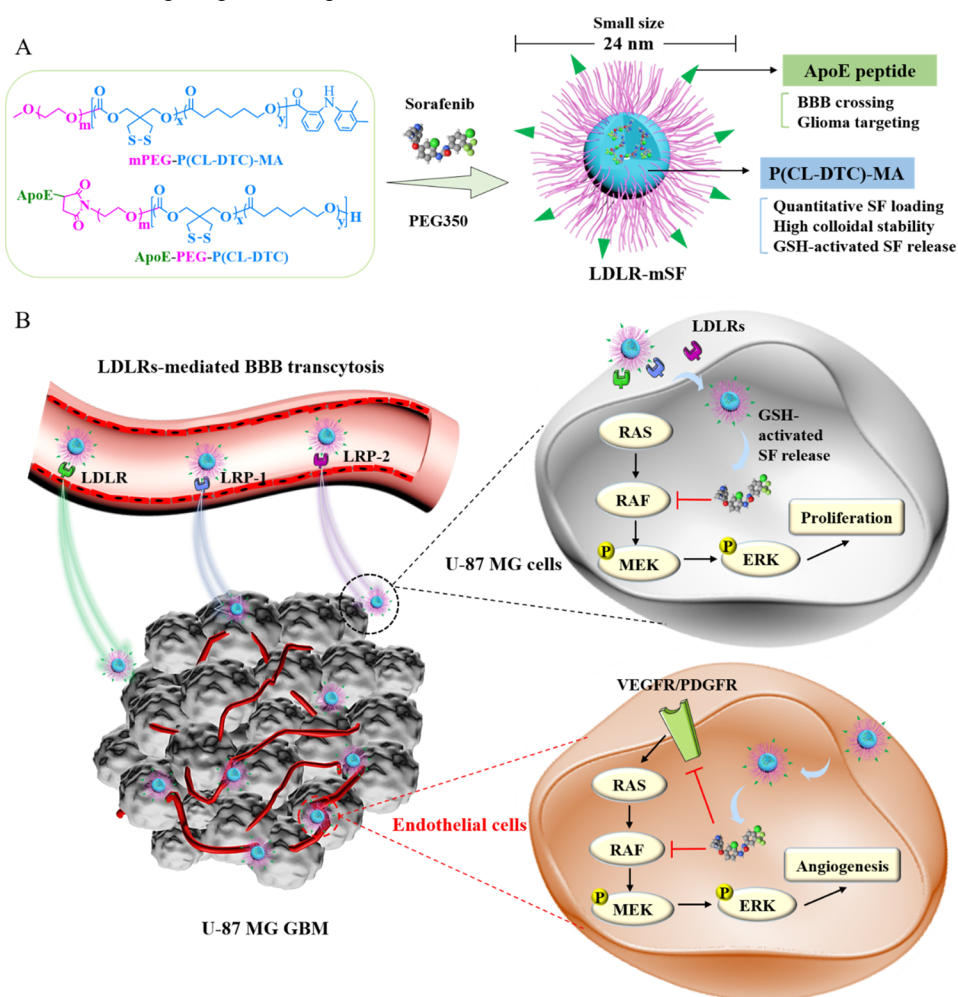
The clinical use of SF is also disturbed by its poor bioavailability and high and frequent dosing that causes toxicity issues.<sup>9,19</sup> Several nanosystems such as lipopolyplex and hydrogels have been studied to enhance SF delivery for hepatocellular carcinoma.<sup>20,21</sup> Notably, intratumoral administration of SF-loaded lipid nanocapsules was reported to efficiently treat GBM xenografts.<sup>22</sup>

The overexpression of receptors such as low-density lipoprotein receptors (LDLRs, including LRP-1, LRP-2, and LDLR), the transferrin receptor, and integrins on BBB and GBM cells provides a unique foundation for enhanced drug delivery to GBM.<sup>23–27</sup> We found that apolipoprotein E peptide (ApoE, sequence: LRKLRKLLLRKLRKLLC), which is the tandem-repeat dimer peptide of the apolipoprotein E protein receptor-binding region, could bind to LDLRs with a high affinity<sup>28</sup> and mediate marked BBB penetration and protein delivery for orthotopic GBM.<sup>29</sup> Herein, we designed and explored small, smart, and LDLR-specific micelles based on the poly(ethylene glycol)-*b*-poly( $\epsilon$ -caprolactone-*co*-dithiolane tri-

Received: August 24, 2021  
Revised: October 14, 2021  
Published: October 22, 2021



**Scheme 1. Schematic Illustration of Small, Smart, and LDLR-Specific Micelles Loading SF (LDLR-mSF) (A) and Its Enhanced BBB Penetration and Tumor Targeting Resulting in Better Inhibition of U-87 MG Tumor Cells and Tumor Angiogenesis (B)**



methylene carbonate)-mefenamate (PEG-P(CL-DTC)-MA) copolymer to efficiently load SF (LDLR-mSF) and to improve SF therapy of GBM by enhancing BBB penetration, GBM accumulation, and cell uptake (Scheme 1). The disulfide-crosslinked nanomedicines based on PEG-P(CL-DTC) have exhibited excellent *in vivo* stability and triggered the drug release property upon cytosol entry, affording great antitumor efficacy.<sup>30,31</sup> Further modifying PEG-P(CL-DTC) with MA, an anti-inflammatory analgesic agent, could endow stable SF loading into the micelles.<sup>32</sup> Interestingly, our results showed that LDLR-mSF induced an order of magnitude stronger anti-GBM activity toward U-87 MG cells and significantly enhanced tumor repression and survival rates of orthotopic U-87 MG-Luc tumor-bearing mice than free SF and non-LDLR mSF controls by inducing GBM cell apoptosis and inhibiting tumor angiogenesis.

## EXPERIMENTAL SECTION

**Fabrication of SF-Loaded Micelles.** SF-loaded ApoE peptide-functionalized micelles (LDLR-mSF) were fabricated by adding a predetermined PEG350 solution of PEG-P(CL-DTC)-MA, ApoE-PEG-P(CL-DTC), and SF into PB and mixing uniformly. The ApoE peptide content on LDLR-mSF was facily controlled by adjusting the molar ratio of ApoE-PEG-P(CL-DTC) and PEG-P(CL-DTC)-MA in the preparation. In a representative example of 2.5% LDLR-mSF, 50  $\mu$ L of PEG350 solution of ApoE-PEG-P(CL-DTC) and

PEG-P(CL-DTC)-MA at 2.5/97.5 mol/mol (corresponding weight ratio: 4.8/95.2 and total polymer concentration: 200 mg/mL) containing SF (SF concentration: 50 mg/mL) was added into PB (950  $\mu$ L, 10 mM, pH 7.4) and carefully mixed using a pipette tip to obtain a uniform dispersion. The dispersions were then dialyzed against PB for 5 h. The drug loading content (DLC) and efficiency (DLE) of SF were measured using UV-vis spectroscopy (absorbance at 269 nm). The drug loading efficiencies of SF-loaded micelles with different ApoE densities were >97% (97.1, 98.2, 98.6, and 98.2% for 1, 2.5, 5, and 7.5% LDLR-mSF, respectively) at a theoretical loading content of 9.1 wt %. Since PEG350 is a safe excipient, in the following experiments, PEG350 was not removed. The size, size distribution, and zeta potentials were measured with a Zetasizer Nano-ZS (Malvern Instruments). LDLR-mSF was stained with phosphotungstic acid and observed using transmission electron microscopy (HITACHI HT7700). The colloidal stability of mSF and LDLR-mSF upon dilution and storage at room temperature was studied by tracking the changes in size and size distribution using a Zetasizer Nano-ZS. The SF loading stability was determined by measuring the SF leakage during storage using UV-vis spectroscopy.

Cy5-labeled 2.5% LDLR-mSF was prepared similarly from ApoE-PEG-P(CL-DTC), PEG-P(CL-DTC)-Cy5, and PEG-P(CL-DTC)-MA, and a molar ratio of 2.5/0.5/97.0 was used.

**In Vitro Transport Study of LDLR-mSF Using a BBB-Mimicking bEnd.3 Cell Monolayer.** Briefly,  $1.0 \times 10^5$  bEnd.3 cells were seeded on polycarbonate 24-well transwell membranes with a mean pore size of 1.0  $\mu$ m and surface area of 0.33 cm<sup>2</sup> (Corning). The bottom well was filled with 900  $\mu$ L of DMEM. The transwell was

**Table 1.** Characterization of mSF and LDLR-mSF

formulation	DLC (wt %) <sup>a</sup>		DLE <sup>a</sup> (%)	size <sup>b</sup> (nm)	PDI <sup>b</sup>	Zeta potential <sup>c</sup> (mV)
	theoretical	determined <sup>a</sup>				
mSF	4.8	4.8	100.0	24.6 ± 0.1	0.14 ± 0.03	0.7 ± 0.2
	9.1	8.9	98.2	24.5 ± 0.1	0.16 ± 0.02	-1.8 ± 0.6
LDLR-mSF	9.1	8.9	98.2	27.4 ± 0.5	0.16 ± 0.02	-3.1 ± 0.9

<sup>a</sup>Determined using a UV-vis spectrometer. <sup>b</sup>Determined by DLS at 25 °C in PB (pH 7.4, 10 mM). <sup>c</sup>Determined by electrophoresis at 25 °C in PB (pH 7.4, 10 mM).

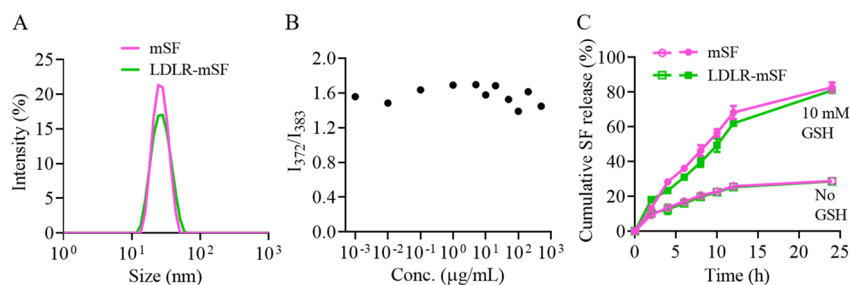


**Figure 1.** (A) Size and size distribution profiles of mSF and LDLR-mSF. (B) Fluorescence intensity ratio of  $I_{372}$  to  $I_{383}$  as a function of micelle concentrations. (C) *In vitro* release SF profiles from mSF and LDLR-mSF in PB (pH 7.4, 10 mM) with or without 10 mM GSH ( $n = 3$ ).

cultured in DMEM medium in a humidified atmosphere containing 5% CO<sub>2</sub> at 37 °C. The integrity of the monolayer was ensured by growing the bEnd.3 cell layer with a *trans*-endothelial electrical resistance (TEER) of > 200 Ω·cm<sup>2</sup> throughout the transcytosis experiment as determined with an epithelial voltmeter (Millicell-RES, Millipore, USA).

mSF and LDLR-mSF with different ApoE densities (1, 2.5, 5, and 7.5%) were added to the donor chamber (SF concentration: 3 μg/mL). At 6, 12, and 24 h, the medium in the bottom chamber was collected to quantify the transcytosed SF using HPLC, and an equal volume of fresh medium was added. The transport ratio was defined as the ratio of SF in the bottom chamber to the total SF added in the donor chamber ( $n = 3$ ).

**Receptor-Mediated Cell Uptake, Apoptosis, and Protein Inhibition of U-87 MG Cells.** The cells were seeded in a 6-well plate ( $3.0 \times 10^5$  cells/well) and cultured in an incubator overnight. For a receptor-mediated cell uptake study, the cells were incubated for 4 h with Cy5-labeled LDLR-mSF (ApoE densities of 1.0–7.5 mol %) or mSF-Cy5 (Cy5:2 nM) at 37 °C before digestion and prepared for flow cytometric analysis ( $n = 3$ ).

For the apoptosis study, the cells were incubated for 4 h with LDLR-mSF, mSF, or SF (SF: 3 μg/mL) and 44 h with drug-free medium. The medium and cells were centrifuged, and the cell pellet was washed twice with PBS and stained with Annexin V-AF647 and PI for 20 min in the dark and subjected to flow cytometry measurements within 15 min.

The inhibition of SF formulations on MAPK signaling pathway by downregulating downstream pERK was studied using western blot in U-87 MG cells. The cells were cultured in a 6-well plate ( $3.0 \times 10^5$  cells/well) overnight, then with LDLR-mSF, mSF, or SF (3 μg/mL) for 4 h, and finally with fresh medium for 44 h. The cells were lysed with RIPA buffer and treated with protocol in the Supporting Information before monitoring the luminescence signals using Super Signal ECL.

**Cytotoxicity Assays.** The *in vitro* antitumor effect of SF, mSF, and LDLR-mSF was evaluated by MTT assays ( $n = 4$ ). U-87 MG cells were cultured in a 96-well plate ( $3.0 \times 10^3$  cells/well) overnight. A total of 10 μL of SF, mSF, or LDLR-mSF with an ApoE density of 2.5, 5.0, or 7.5 mol % and SF concentration from 0.078 to 40 μg/mL was added and incubated for 4 h. Then, the cells were further cultured in drug-free medium for 44 h. Subsequently, 10 μL of MTT (5 mg/mL) was supplemented, and 150 μL of DMSO was used to dissolve formazan generated by live cells before measuring the absorbance (at 570 nm) using a microplate reader. The cell viability (%) was

determined compared with PBS-treated control wells (as 100%). The cytotoxicity of empty micelles (non-LDLR m and LDLR-m) at concentrations of 0.5, 1.0, and 2.0 mg/mL to U-87 MG cells was assessed similarly ( $n = 4$ ).

***In Vivo* Pharmacokinetics, Fluorescence Imaging, and Biodistribution.** Into healthy Balb/c mice (female, 5-week), 200 μL of free SF, mSF, or LDLR-mSF (15 mg of SF/kg) was intravenously (i.v.) injected ( $n = 3$ ). At the preset time points, ca. 60 μL of blood was withdrawn via the retro-orbital sinus. To extract SF, 20 μL of plasma was obtained and immediately incubated at 37 °C with 300 μL of acetonitrile (containing 20 mM DTT) for 24 h. The SF concentration was determined using HPLC based on a calibration curve got from SF solutions of known concentrations treated as the blood samples. The SF concentration was plotted *versus* time, and the elimination half-lives and area under the curve (AUC) were analyzed using PK Solver software.

To establish an orthotopic U-87 MG mouse model, luciferase-transfected U-87 MG cells (U-87 MG-Luc) were first injected into Balb/c nude mice (female, 6 week) subcutaneously. At a tumor size of 300–500 mm<sup>3</sup>, the tumors were cut into small pieces and stereotactically injected into the right striatum using a 26-gauge syringe with the bregma as the origin of coordinates (coordinates: 1.0 mm latter, 2.0 mm lateral, and 3.0 mm deep). The syringe remained there for 5 min before withdrawal. For *in vivo* imaging, on day 10 after implantation, Cy5-labeled mSF or LDLR-mSF (15 mg of SF/kg, 0.5 μg of Cy5 per mouse) was i.v. injected. At certain time points, the mice were scanned using an IVIS II system.

For the biodistribution study, on day 10 after implantation, 200 μL of free SF, mSF, or LDLR-mSF (15 mg of SF/kg) was i.v. injected into the orthotopic model ( $n = 3$ ). After 8 h, the mice were sacrificed and major organs, the brain, and tumors were dissected. DMSO solution (containing 20 mM DTT) was added and homogenized to extract SF. SF was quantified by HPLC based on calibration curves obtained from SF solutions of known concentrations in the presence of organs treated as samples.

***In Vivo* Antiglioma Effects of SF Formulations on the Orthotopic U-87 MG Model.** On day 4, 6, 8, 10, 12, and 14 after tumor inoculation, mice bearing orthotopic U-87 MG tumors were randomly grouped and i.v. administered with 200 μL of free SF, mSF, LDLR-mSF (15 mg of SF/kg), and PBS ( $n = 7$ ). On day 4, 8, and 15, luciferin potassium salt (75 mg/kg) was i.p. injected, and within 15 min, the bioluminescence of animals was measured to monitor the tumor progression. Mice were weighed every two days. The bioluminescence intensity and body weight were relative to their

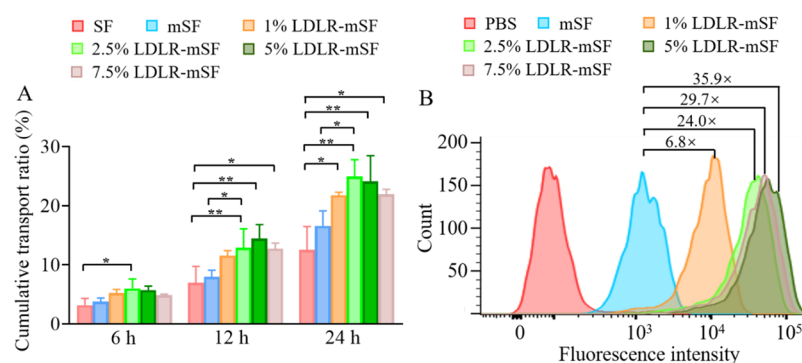


**Figure 2.** Receptor-mediated BBB transcytosis and U-87 MG cell uptake of LDLR-mSF with an ApoE density of 1, 2.5, 5, or 7.5%. (A) Transport ratio of SF, mSF, and LDLR-mSF across the bEnd.3 cell monolayer at different incubation times. (B) Endocytosis of Cy5-labeled LDLR-mSF by U-87 MG cells at 4 h of incubation measured by flow cytometry.

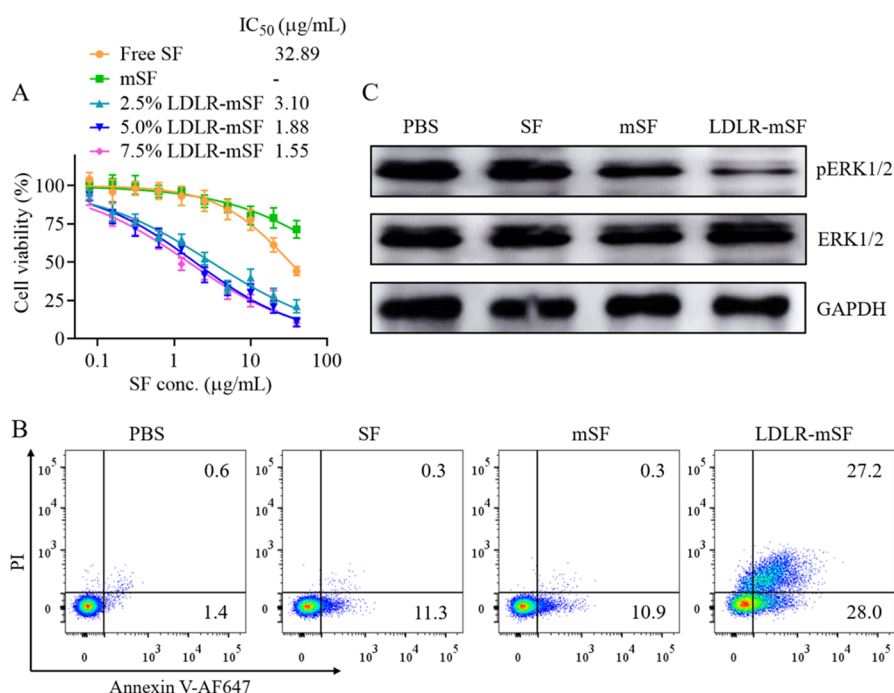


**Figure 3.** Antitumor activity and downregulation of the pERK protein of LDLR-mSF, mSF, and free SF in U-87 MG cells (4 h of incubation with drug followed by 44 h of incubation in drug-free fresh medium). (A) MTT assays of cytotoxicity ( $n = 4$ ). (B) Flow cytometry analysis of apoptosis (SF: 3  $\mu\text{g/mL}$ ). (C) Western blot analysis of the pERK protein (SF: 3  $\mu\text{g/mL}$ ).

values on day 4. On day 18, one mouse of each group was euthanized; major organs, the brain, and tumors were collected and sliced, and tumor-bearing brains and major organs were stained with hematoxylin and eosin (H&E). In addition, tumor-containing brain slices were deparaffined with xylene and rehydrated with gradient ethanol, antigen was retrieved with Tris-EDTA (pH 9.0); then, apoptotic cells were marked by terminal deoxynucleotidyl transferase-mediated nick end labeling (TUNEL). The pERK protein was stained with primary rabbit mAb pERK and secondary Alexa Fluor 633-conjugated goat anti-rabbit IgG. The VEGFR protein was stained with primary rabbit mAb VEGFR and secondary Alexa Fluor 633-conjugated goat anti-rabbit IgG. The blood vessels in the tumors were stained with primary rat polyclonal antibody CD31 and secondary Alexa Fluor 488-conjugated donkey anti-rat IgG. The tissue slices were observed using a fluorescence microscope. The rest of the mice were used for monitoring survival rates ( $n = 6$ ).

**Statistical Analysis.** Data were represented as mean  $\pm$  SD. The significance of differences among groups was analyzed using GraphPad Prism 8 by One-way ANOVA using Tukey's post-test, and survival analysis was done using the log-rank (Mantel-Cox) test. \* $p < 0.05$ , \*\* $p < 0.01$ , \*\*\* $p < 0.001$ , and \*\*\*\* $p < 0.0001$ .

## RESULTS AND DISCUSSION

**Synthesis of the Block Copolymers.** The present study aimed to develop small, smart, and LDLR-specific micelles to enhance SF delivery to GBM, for which a PEG-P(CL-DTC)-MA copolymer ( $M_n = 4.2$  kg/mol) with the mefenamate terminal group and ApoE-PEG-P(CL-DTC) were designed and synthesized. DTC-containing micelles were found to be highly stable as a result of core-disulfide crosslinking.<sup>33,34</sup> MA was introduced to improve SF loading and micellar stability, *via* the principle of  $\pi$ - $\pi$  stacking as reported previously for different systems and anticancer drugs.<sup>32</sup> PEG-P(CL-DTC)-MA was obtained *via* copolymerization of DTC and CL (1/1, w/w) using mPEG ( $M_n = 2.0$  kg/mol) and organocatalyst DPP,<sup>35</sup> followed with esterification with mefenamic acid.<sup>32</sup> PEG-P(CL-DTC) had prescribed the composition and molecular weight as determined by <sup>1</sup>H NMR (Figure S1A) and narrow polydispersity index ( $M_w/M_n = 1.1$ ) as measured by GPC. PEG-P(CL-DTC)-MA displayed typical signals of

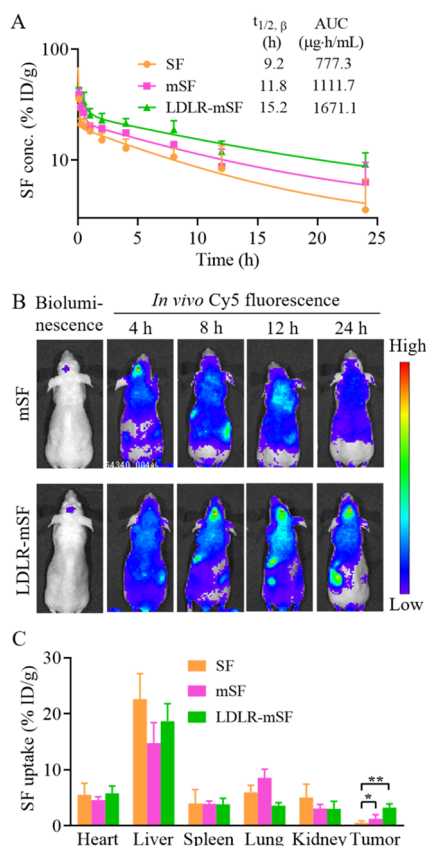


**Figure 4.** Pharmacokinetics and biodistribution of LDLR-mSF, mSF, and SF in mice. (A) Pharmacokinetics determined using HPLC ( $n = 3$ ). (B) *In vivo* NIR imaging using Cy5-labeled micelles and (C) biodistribution study determined by HPLC (15 mg of SF/kg) at 8 h after injection ( $n = 3$ ) in orthotopic U-87 MG-bearing mice.

MA at  $\delta$  6.67–9.20 in the  $^1\text{H}$  NMR spectrum and an MA functionality of over 95% (Figure S1B).

ApoE-PEG-P(CL-DTC) was produced through Michael addition reaction between LRKLRKLLLRKLRKLLC peptide and Mal-PEG-P(CL-DTC) ( $M_n = 5.6$  kg/mol and  $M_w/M_n = 1.2$ , Figure S2A). The PEG in ApoE-PEG-P(CL-DTC) had a higher  $M_n$  than that in PEG-P(CL-DTC)-MA (3.4 vs 2.0 kg/mol) to ensure the exposure of the ApoE ligand.<sup>29,32</sup> The  $^1\text{H}$  NMR spectrum showed characteristic peaks of the ApoE peptide at  $\delta$  7.09–8.68 and 0.78–0.92 and complete disappearance of the Mal signal at  $\delta$  7.00 (Figure S2B). Micro-BCA assay confirmed a high ApoE functionality of >95%.

**Fabrication of LDLR-mSF.** LDLR-mSF was produced by addition of ApoE-PEG-P(CL-DTC) and PEG-P(CL-DTC)-MA (final ApoE density of 1, 2.5, 5, or 7.5%) and SF in PEG 350 to an aqueous solution. As an example, 2.5% LDLR-mSF realized almost quantitative encapsulation of SF at a theoretical drug loading content (DLC) of 9.1 wt % (Table 1). The TEM image confirmed the small size and uniform distribution of LDLRs-mSF (Figure S3). In sharp contrast, micelles made of PEG-P(CL-DTC) (without MA) revealed a markedly inferior drug loading efficiency (DLE) of 46.1%, supporting that MA plays a critical role in SF loading. All LDLR-mSF had small sizes (*ca.* 24 nm) with narrow size distribution (Figure 1A) and a near-neutral surface charge (Table 1). The analysis of critical micellar concentration (CMC) using pyrene as a fluorescent probe exposed that there was no sharp transition of  $I_{372}/I_{383}$ ,

and no dissociation occurred at micelle concentrations from  $10^{-3}$  to  $10^3$   $\mu\text{g}/\text{mL}$  (Figure 1B), pointing to the disulfide crosslinking formed during the preparation. Accordingly, mSF and LDLR-mSF exhibited great colloidal stability upon dilution to 50  $\mu\text{g}/\text{mL}$  (Figure S4A,B) and colloidal stability and drug loading stability at storage for at least 7 days at room temperature (Figure S4C,D). The release studies showed a markedly accelerated release of SF from LDLR-mSF under a 10 mM GSH environment in 24 h (Figure 1C). The non-LDLR mSF exhibited nearly the same physicochemical and release properties as LDLR-mSF. The GSH solution (10 mM) was used to mimic the intracellular reductive conditions since the concentration of reductive agents in the cytoplasm (mainly GSH) is 2–3 orders of magnitude higher than that of the extracellular environment and the blood. The triggered SF release from LDLR-mSF and mSF with 10 mM GSH further confirmed the de-crosslinking and dissociation of the DTC-containing micelles due to the disulfide cleavage into free thiols,<sup>33,36</sup> implying the stability during circulation and fast drug release once internalized by GBM cells of LDLR-mSF and mSF.

**Receptor-Mediated BBB Transcytosis and U-87 MG Cell Uptake.** To efficiently kill GBM cells and inhibit angiogenesis, SF has to cross the BBB and be delivered to the tumor site. The BBB transcytosis behavior of LDLR-mSF was investigated using the bEnd.3 murine endothelial cell monolayer as a BBB model. LDLR-mSF with different ApoE densities (1, 2.5, 5, and 7.5%) was added to the donor chamber, and LDLR-mSF penetrated through the monolayer into the bottom of a 24-well plate was quantified using HPLC. The results showed clearly a higher transport ratio of 2.5% LDLR-mSF than free SF and mSF (Figure 2A), but there was no statistical difference among LDLR-mSF with different ApoE densities (1–7.5%). In spite of the tight junction and lack of receptor-mediated transcytosis, mSF and free SF could also cross the BBB to some lower degree, possibly through nonreceptor-mediated transcytosis.<sup>37</sup> This enhanced transcytosis of LDLR-mSF supports the high affinity of ApoE to LDLRs on the BBB.<sup>29,38</sup> LDLR-mSF and mSF showed no cytotoxicity to bEnd.3 cells under the same conditions (Figure S5). Moreover, the endocytosis of Cy5-labeled LDLR-mSF was studied in U-87 MG cells. Flow cytometric results illustrated a significantly increased uptake of mSF by ApoE, in which 6.8-, 24.0-, 35.9-, and 29.7-fold higher endocytosis was observed at 1, 2.5, 5, and 7.5% ApoE density, respectively (Figure 2B), in line with overexpression of LDLRs in U-87 MG cells<sup>39</sup> and receptor-mediated endocytosis of LDLR-mSF by GBM cells.

**Antitumor Activity of LDLR-mSF and Downregulation of the pERK Protein.** To investigate the antitumor potency of LDLR-mSF, MTT and apoptotic assays were conducted in U-87 MG cells. Interestingly, LDLR-mSF with 2.5, 5, and 7.5% ApoE all showed an order of magnitude stronger antitumor activity than free SF and nontargeted mSF ( $\text{IC}_{50} = 1.6\text{--}3.1$   $\mu\text{g}/\text{mL}$  vs  $>32$   $\mu\text{g}/\text{mL}$ ) (Figure 3A). The low cytotoxicity of mSF to U-87 MG cells could be probably ascribed to the lack of LDLR-mediated endocytosis, resulting in a low intracellular micellar concentration, in line with the cellular uptake results (Figure 2B). Empty micelles (LDLR-m) did not show cytotoxicity to the cells even at an LDLR-m concentration of 2 mg/mL (Figure S6). Considering the best performance in BBB transcytosis and endocytosis and cytotoxicity in U-87 MG cells, LDLR-mSF with 2.5% ApoE was chosen for further studies. The apoptotic assays displayed

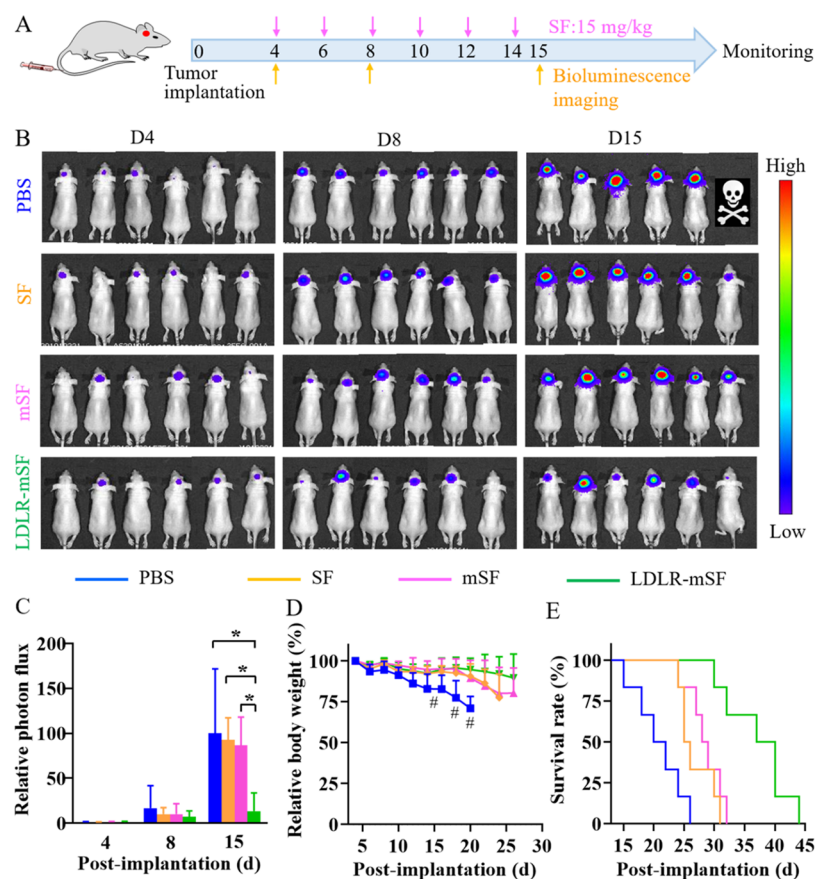


**Figure 5.** *In vivo* therapy of orthotopic U-87 MG-bearing mice with SF, mSF, and LDLR-mSF (15 mg of SF/kg) ( $n = 6$ ). (A) Treatment scheme. (B) *In vivo* bioluminescence images on day 4, 8, and 15 after tumor implantation. (C) Relative tumor bioluminescence intensity. (D) Relative body weight. (E) Kaplan–Meier survival curves. LDLR-mSF vs PBS,  $***p < 0.001$ ; LDLR-mSF vs SF or mSF,  $**p < 0.01$ .

that LDLR-mSF caused 55.2% cell apoptosis, while free SF and mSF induced only  $\sim 10\%$  apoptosis of tumor cells (Figure 3B). We using western blot further studied the expression of the pERK protein in LDLR-mSF-treated U-87 MG cells. SF was reported to induce apoptosis by inhibiting the extremely active MAPK signaling pathway in tumor cells.<sup>32,40</sup> The results showed that LDLR-mSF at  $3 \mu\text{g}$  of SF/mL greatly inhibited ERK phosphorylation (Figure 3C). The pERK1/2 protein level of the LDLR-mSF group was 2.1- and 1.6-fold lower than that of free SF and mSF controls, respectively. These results verify that LDLR-mSF possesses high specificity and potency to GBM cells by blocking the RAF-MEK-ERK (MAPK) pathway.

**Pharmacokinetics and Biodistribution of LDLR-mSF in Mice.** The pharmacokinetic studies in healthy mice showed that both LDLR-mSF and mSF had a prolonged elimination half-life ( $t_{1/2,\beta} = 15.2$  and  $11.8$  h, respectively) and larger area under the curve (AUC) than free SF (Figure 4A). The slower elimination of LDLR-mSF than mSF might be ascribed to its longer PEG chains ( $3.4$  vs  $2.0$  kg/mol).<sup>41</sup> The *in vivo* near-infrared (NIR) imaging of the mice bearing orthotopic U-87 MG Luc tumors exhibited pronounced Cy5 fluorescence in the tumor at 8–24 h after injection of Cy5-labeled LDLR-mSF compared to mSF (Figure 4B). We further quantified SF levels in major organs at 8 h after administration of SF formulations into orthotopic U-87 MG-bearing mice. Notably, LDLR-mSF reached a SF tumor accumulation of 3.3% ID/g, which was 6.0- and 2.5-fold that of free SF ( $**p$ ) and non-LDLR mSF ( $*p$ ) groups, respectively (Figure 4C). Importantly, negligible

SF was detected in the normal brain tissue of mice. These results indicated that LDLR-mSF is able to cross the BBB and selectively target GMB tumors. Hematoxylin–eosin (H&E) staining showed no damage of LDLR-mSF to all major organs (Figure S7), which is possibly due to the specific action of SF and safe dose used in this study.<sup>42,43</sup>

**Targeted Treatment of Mice Bearing Orthotopic U-87 MG-Luc Xenografts.** Inspired by its BBB-crossing ability, high selectivity, and potency to U-87 MG cells, we further evaluated the therapeutic effect of LDLR-mSF toward the orthotopic model. On day 4 after tumor implantation, the mice were scanned using an IVIS imaging system to get the initial bioluminescence and divided into four groups: PBS, SF, mSF, and LDLR-mSF (15 mg of SF/kg). SF formulations were *i.v.* injected on day 4, 6, 8, 10, 12, and 14, respectively (Figure 5A). Clinically, SF is orally dosed at 400 mg per time (equivalent to 50–60 mg of SF/kg in mice) and twice a day. Such a frequent and high-dosing scheme often causes toxicity and modest efficacy. In this study, LDLR-mSF was applied at a low dose of 15 mg of SF/kg every two days to achieve good therapeutic efficacy without causing side effects. Figure 5B shows markedly stronger tumor inhibition of LDLR-mSF than SF and mSF. The semiquantification of tumor bioluminescence revealed significantly lower U-87 MG tumor bioluminescence in the LDLR-mSF group compared to PBS, SF, and mSF groups on D15 ( $*p$ , Figure 5C). The mice in the PBS group showed a significant body weight decrease within 20 days due to invasion of GBM, and one mouse died on day 15 (Figure 5D). The LDLR-mSF group exhibited the least

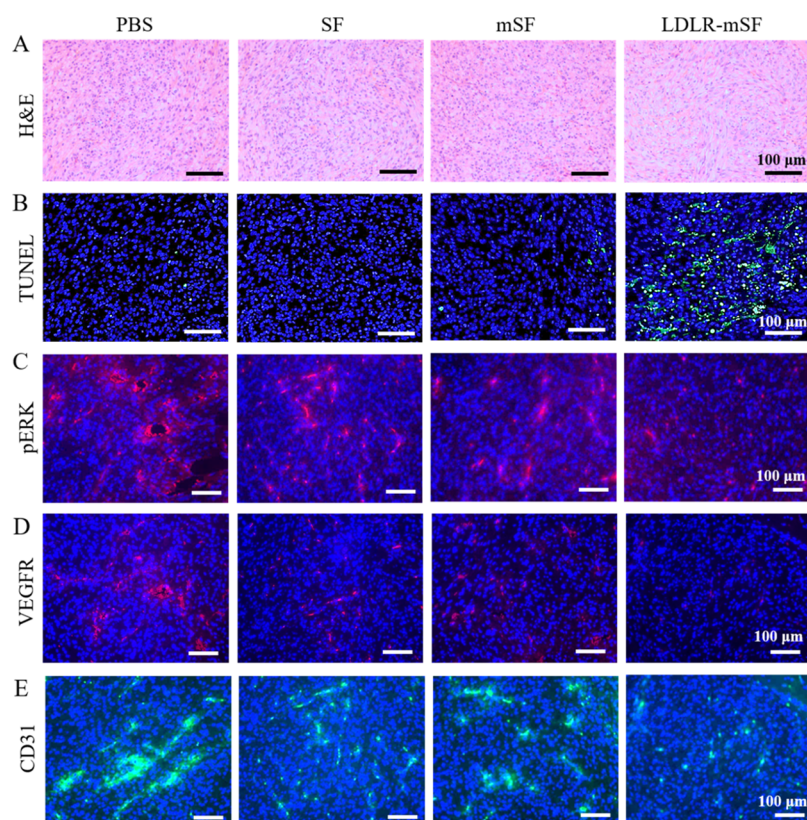


**Figure 6.** Immunohistochemical analyses of the brain tumor on day 16 after implantation treated as in Figure 5 and stained with (A) H&E, (B) TUNEL (apoptotic cells: green fluorescence), (C) anti-pERK antibody (red fluorescence), (D) anti-VEGFR antibody (red fluorescence), and (E) anti-CD31 antibody (green fluorescence).

body weight loss among all groups, supporting its effective GBM inhibition and low systemic toxicity (Figure S7). The survival curves of mice exhibited that LDLR-mSF significantly extended the median survival time (MST) to 37 days from merely 20 days for the PBS group (\*\**p*, Figure 5E). In comparison, free SF and nontargeted mSF caused only a moderate increase in MST.

On day 16, one mouse of each group was euthanized, and the tumor-containing brain was isolated for immunohistochemical analyses. H&E staining images showed that tumor cell density in the LDLR-mSF group was the lowest among all groups, and plenty of tumor cells underwent apoptosis (Figure 6A). Further TUNEL assays certified that LDLR-mSF brought about the most extensive tumor cell apoptosis (green fluorescence) (Figure 6B). Moreover, the analyses of pERK proteins in the tumor tissues revealed a reduced pERK expression in the tumors of the LDLR-mSF group compared with free SF and mSF groups (Figure 6C). Notably, LDLR-mSF showed also a clear antiangiogenic effect with a significantly decreased VEGFR expression (Figure 6D) and the number of blood vessels (Figure 6E) in the tumor tissue. These results conclude that LDLR-mSF augments SF delivery to GBM and causes not only selective inhibition of GBM cells but also reduction of tumor angiogenesis, leading to potent SF therapy of orthotopic GBM in mice.

## CONCLUSIONS

We have demonstrated that small, smart, and LDLR-specific micelles (LDLR-m) are able to efficiently load and deliver SF across the BBB and selectively into GBM tumors, resulting in

superior tumor inhibition and survival benefits. Notably, LDLR-m serves not only to improve the pharmacokinetics and biodistribution of SF but also to markedly enhance its selectivity and antitumor activity toward GBM cells. This is a first report on the development of targeted SF therapy for GBM. Unlike most cytotoxic drugs, SF as a targeted molecular drug is essentially nontoxic at the dosage used in this study. LDLR-mSF with easy fabrication and favorable biophysical properties provides a new and advanced therapeutic strategy for GBM.

## ASSOCIATED CONTENT

### Supporting Information

The Supporting Information is available free of charge at <https://pubs.acs.org/doi/10.1021/acs.biomac.1c01103>.

Materials and characterizations; synthesis and  $^1\text{H}$  NMR spectra of copolymers; critical micelle concentration (CMC) determination; *in vitro* SF release behavior; western blot assay; TEM and stability study of LDLR-mSF; cytotoxicity of LDLR-mSF toward bEnd.3 cells and of empty LDLR-m toward U-87 MG cells (PDF)

## AUTHOR INFORMATION

### Corresponding Authors

Fenghua Meng – Biomedical Polymers Laboratory, College of Chemistry, Chemical Engineering and Materials Science, and State Key Laboratory of Radiation Medicine and Protection, Soochow University, Suzhou 215123, P. R. China; [orcid.org/0000-0002-8608-7738](https://orcid.org/0000-0002-8608-7738); Email: [fhmeng@suda.edu.cn](mailto:fhmeng@suda.edu.cn)

Zhiyuan Zhong – Biomedical Polymers Laboratory, College of Chemistry, Chemical Engineering and Materials Science, and State Key Laboratory of Radiation Medicine and Protection, Soochow University, Suzhou 215123, P. R. China;

ORCID: [orcid.org/0000-0003-4175-4741](https://orcid.org/0000-0003-4175-4741); Email: [zyzhong@suda.edu.cn](mailto:zyzhong@suda.edu.cn)

## Authors

Jingjing Wei – Biomedical Polymers Laboratory, College of Chemistry, Chemical Engineering and Materials Science, and State Key Laboratory of Radiation Medicine and Protection, Soochow University, Suzhou 215123, P. R. China

Yifeng Xia – Biomedical Polymers Laboratory, College of Chemistry, Chemical Engineering and Materials Science, and State Key Laboratory of Radiation Medicine and Protection, Soochow University, Suzhou 215123, P. R. China

Dawei Ni – Biomedical Polymers Laboratory, College of Chemistry, Chemical Engineering and Materials Science, and State Key Laboratory of Radiation Medicine and Protection, Soochow University, Suzhou 215123, P. R. China

Xinyun Qiu – Biomedical Polymers Laboratory, College of Chemistry, Chemical Engineering and Materials Science, and State Key Laboratory of Radiation Medicine and Protection, Soochow University, Suzhou 215123, P. R. China

Complete contact information is available at:

<https://pubs.acs.org/10.1021/acs.biomac.1c01103>

## Notes

The authors declare no competing financial interest.

## ACKNOWLEDGMENTS

This work is supported by research grants from the National Natural Science Foundation of China (NSFC 51773146, 51861145310, 51633005, and 52033006).

## REFERENCES

- (1) Neftel, C.; Laffy, J.; Filbin, M. G.; Hara, T.; Shore, M. E.; Rahme, G. J.; Richman, A. R.; Silverbush, D.; Shaw, M. L.; Hebert, C. M.; Dewitt, J.; Gritsch, S.; Perez, E. M.; Gonzalez Castro, L. N.; Lan, X.; Druck, N.; Rodman, C.; Dionne, D.; Kaplan, A.; Bertalan, M. S.; Small, J.; Pelton, K.; Becker, S.; Bonal, D.; Nguyen, Q.-D.; Servis, R. L.; Fung, J. M.; Mylvaganam, R.; Mayr, L.; Gojo, J.; Haberler, C.; Geyerregger, R.; Czech, T.; Slavic, I.; Nahed, B. V.; Curry, W. T.; Carter, B. S.; Wakimoto, H.; Brastianos, P. K.; Batchelor, T. T.; Stemmer-Rachamimov, A.; Martinez-Lage, M.; Frosch, M. P.; Stamenkovic, I.; Riggi, N.; Rheinbay, E.; Monje, M.; Rozenblatt-Rosen, O.; Cahill, D. P.; Patel, A. P.; Hunter, T.; Verma, I. M.; Ligon, K. L.; Louis, D. N.; Regev, A.; Bernstein, B. E.; Tirosch, I.; Suvà, M. L. An integrative model of cellular states, plasticity, and genetics for glioblastoma. *Cell* **2019**, *178*, 835–849.
- (2) Wen, P. Y.; Weller, M.; Lee, E. Q.; Alexander, B. M.; Barnholtz-Sloan, J. S.; Barthel, F. P.; Batchelor, T. T.; Bindra, R. S.; Chang, S. M.; Chiocca, E. A.; Cloughesy, T. F.; DeGroot, J. F.; Galanis, E.; Gilbert, M. R.; Hegi, M. E.; Horbinski, C.; Huang, R. Y.; Lassman, A. B.; Le Rhun, E.; Lim, M.; Mehta, M. P.; Mellinghoff, I. K.; Minniti, G.; Nathanson, D.; Platten, M.; Preusser, M.; Roth, P.; Sanson, M.; Schiff, D.; Short, S. C.; Taphoorn, M. J. B.; Tonn, J.-C.; Tsang, J.; Verhaak, R. G. W.; von Deimling, A.; Wick, W.; Zadeh, G.; Reardon, D. A.; Aldape, K. D.; van den Bent, M. J. Glioblastoma in adults: A Society for Neuro-Oncology (SNO) and European Society of Neuro-Oncology (EANO) consensus review on current management and future directions. *Neuro Oncol.* **2020**, *22*, 1073–1113.
- (3) Rajaratnam, V.; Islam, M.; Yang, M.; Slaby, R.; Ramirez, H.; Mirza, S. Glioblastoma: Pathogenesis and current status of chemotherapy and other novel treatments. *Cancers* **2020**, *12*, 937.
- (4) Moore, A. R.; Rosenberg, S. C.; McCormick, F.; Malek, S. RAS-targeted therapies: Is the undruggable drugged? *Nat. Rev. Drug Discovery* **2020**, *19*, 533–552.
- (5) Erkes, D. A.; Cai, W.; Sanchez, I. M.; Purwin, T. J.; Rogers, C.; Field, C. O.; Berger, A. C.; Hartsough, E. J.; Rodeck, U.; Alnemri, E. S.; Aplin, A. E. Mutant BRAF and MEK inhibitors regulate the tumor immune microenvironment via pyroptosis. *Cancer Discov.* **2020**, *10*, 254–269.
- (6) Tian, T.; Li, X.; Zhang, J. mTOR signaling in cancer and mTOR inhibitors in solid tumor targeting therapy. *Int. J. Mol. Sci.* **2019**, *20*, 755.
- (7) Alzahrani, A. S. PI3K/Akt/mTOR inhibitors in cancer: At the bench and bedside. *Semin. Cancer Biol.* **2019**, *59*, 125–132.
- (8) Amani, V.; Prince, E. W.; Alimova, I.; Balakrishnan, I.; Birks, D.; Donson, A. M.; Harris, P.; Levy, J. M. M.; Handler, M.; Foreman, N. K.; Venkataraman, S.; Vibhakar, R. Polo-like Kinase 1 as a potential therapeutic target in diffuse intrinsic pontine glioma. *BMC Cancer* **2016**, *16*, 647.
- (9) Nghiemphu, P. L.; Ebiana, V. A.; Wen, P.; Gilbert, M.; Abrey, L. E.; Lieberman, F.; DeAngelis, L. M.; Robins, H. I.; Yung, W. K. A.; Chang, S.; Drappatz, J.; Mehta, M. P.; Levin, V. A.; Aldape, K.; Dancey, J. E.; Wright, J. J.; Prados, M.; Kuhn, J.; Cloughesy, T. F. Phase I study of sorafenib and tipifarnib for recurrent glioblastoma: NABTC 05-02. *J. Neuro Oncol.* **2018**, *136*, 79–86.
- (10) Zhao, H.-f.; Wang, J.; Shao, W.; Wu, C.-p.; Chen, Z.-p.; To, S.-s. T.; Li, W.-p. Recent advances in the use of PI3K inhibitors for glioblastoma multiforme: current preclinical and clinical development. *Mol. Cancer* **2017**, *16*, 100.
- (11) Liu, N.; Hu, G.; Wang, H.; Li, Z.; Guo, Z. PLK1 inhibitor facilitates the suppressing effect of temozolomide on human brain glioma stem cells. *J. Cell Mol. Med.* **2018**, *22*, 5300–5310.
- (12) Shingu, T.; Holmes, L.; Henry, V.; Wang, Q.; Latha, K.; Gururaj, A. E.; Gibson, L. A.; Doucette, T.; Lang, F. F.; Rao, G.; Yuan, L.; Sulman, E. P.; Farrell, N. P.; Priebe, W.; Hess, K. R.; Wang, Y. A.; Hu, J.; Bögl, O. Suppression of RAF/MEK or PI3K synergizes cytotoxicity of receptor tyrosine kinase inhibitors in glioma tumor-initiating cells. *J. Transl. Med.* **2016**, *14*, 46.
- (13) Roskoski, R., Jr. Properties of FDA-approved small molecule protein kinase inhibitors: A 2020 update. *Pharmacol. Res.* **2020**, *152*, 104609.
- (14) Escudier, B.; Worden, F.; Kudo, M. Sorafenib: key lessons from over 10 years of experience. *Expert Rev. Anticancer Ther.* **2019**, *19*, 177–189.
- (15) Galanis, E.; Anderson, S. K.; Lafky, J. M.; Uhm, J. H.; Giannini, C.; Kumar, S. K.; Kimlinger, T. K.; Northfelt, D. W.; Flynn, P. J.; Jaeckle, K. A.; Kaufmann, T. J.; Buckner, J. C. Phase II study of bevacizumab in combination with sorafenib in recurrent glioblastoma (N0776): A North Central Cancer Treatment Group trial. *Clin. Cancer Res.* **2013**, *19*, 4816–4823.
- (16) Peereboom, D. M.; Ahluwalia, M. S.; Ye, X.; Supko, J. G.; Hilderbrand, S. L.; Phuphanich, S.; Nabors, L. B.; Rosenfeld, M. R.; Mikkelsen, T.; Grossman, S. A. New Approaches Brain Tumor, T. NABTT 0502: a phase II and pharmacokinetic study of erlotinib and sorafenib for patients with progressive or recurrent glioblastoma multiforme. *Neuro Oncol.* **2013**, *15*, 490–496.
- (17) King, J. L.; Benhabbour, S. R. Glioblastoma multiforme—a look at the past and a glance at the future. *Pharmaceutics* **2021**, *13*, 1053.
- (18) Zhou, Y.; Wu, W.; Bi, H.; Yang, D.; Zhang, C. Glioblastoma precision therapy: From the bench to the clinic. *Cancer Lett.* **2020**, *475*, 79–91.
- (19) Howell, J.; Pinato, D. J.; Ramaswami, R.; Bettinger, D.; Arizumi, T.; Ferrari, C.; Yen, C.; Gibbin, A.; Burlone, M. E.; Guaschino, G.; Sellers, L.; Black, J.; Pirisi, M.; Kudo, M.; Thimme, R.; Park, J.-W.; Sharma, R. On-target sorafenib toxicity predicts improved survival in hepatocellular carcinoma: a multi-centre, prospective study. *Aliment. Pharmacol. Ther.* **2017**, *45*, 1146–1155.
- (20) Xu, S.; Ling, S.; Shan, Q.; Ye, Q.; Zhan, Q.; Jiang, G.; Zhuo, J.; Pan, B.; Wen, X.; Feng, T.; Lu, H.; Wei, X.; Xie, H.; Zheng, S.; Xiang, J.; Shen, Y.; Xu, X. Self-activated cascade-responsive sorafenib and

USP22 shRNA co-delivery system for synergetic hepatocellular carcinoma therapy. *Adv. Sci.* **2021**, *8*, 2003042.

(21) Zheng, L.; Li, C. E.; Huang, X.; Lin, X.; Lin, W.; Yang, F.; Chen, T. Thermosensitive hydrogels for sustained-release of sorafenib and selenium nanoparticles for localized synergistic chemoradiotherapy. *Biomaterials* **2019**, *216*, 119220.

(22) Clavreul, A.; Roger, E.; Pourbaghi-Masouleh, M.; Lemaire, L.; Tétaud, C.; Menei, P. Development and characterization of sorafenib-loaded lipid nanocapsules for the treatment of glioblastoma. *Drug Deliv.* **2018**, *25*, 1756–1765.

(23) Gu, W.; Meng, F.; Haag, R.; Zhong, Z. Actively targeted nanomedicines for precision cancer therapy: Concept, construction, challenges and clinical translation. *J. Controlled Release* **2021**, *329*, 676–695.

(24) Song, P.; Song, N.; Li, L.; Wu, M.; Lu, Z.; Zhao, X. Angiopep-2-modified carboxymethyl chitosan-based pH/reduction dual-stimuli-responsive nanogels for enhanced targeting glioblastoma. *Biomacromolecules* **2021**, *22*, 2921–2934.

(25) Kang, S.; Duan, W.; Zhang, S.; Chen, D.; Feng, J.; Qi, N. Muscone/RI7217 co-modified upward messenger DTX liposomes enhanced permeability of blood-brain barrier and targeting glioma. *Theranostics* **2020**, *10*, 4308–4322.

(26) Wu, H.; Lu, H.; Xiao, W.; Yang, J.; Du, H.; Shen, Y.; Qu, H.; Jia, B.; Manna, S. K.; Ramachandran, M.; Xue, X.; Ma, Z.; Xu, X.; Wang, Z.; He, Y.; Lam, K. S.; Zawadzki, R. J.; Li, Y.; Lin, T. Y. Sequential targeting in crosslinking nanotheranostics for tackling the multibarriers of brain tumors. *Adv. Mater.* **2020**, *32*, 1903759.

(27) Dong, C. Y.; Hong, S.; Zheng, D. W.; Huang, Q. X.; Liu, F. S.; Zhong, Z. L.; Zhang, X. Z. Multifunctionalized gold sub-nanometer particles for sensitizing radiotherapy against glioblastoma. *Small* **2021**, *17*, 2006582.

(28) Wang, D.; El-Amouri, S. S.; Dai, M.; Kuan, C.-Y.; Hui, D. Y.; Brady, R. O.; Pan, D. Engineering a lysosomal enzyme with a derivative of receptor-binding domain of apoE enables delivery across the blood-brain barrier. *Proc. Natl. Acad. Sci. U.S.A.* **2013**, *110*, 2999–3004.

(29) Jiang, Y.; Zhang, J.; Meng, F.; Zhong, Z. Apolipoprotein E peptide-directed chimeric polymersomes mediate an ultrahigh-efficiency targeted protein therapy for glioblastoma. *ACS Nano* **2018**, *12*, 11070–11079.

(30) Zhang, C.; Wang, X.; Cheng, R.; Zhong, Z. A6 peptide-tagged core-disulfide-cross-linked micelles for targeted delivery of proteasome inhibitor carfilzomib to multiple myeloma in vivo. *Biomacromolecules* **2020**, *21*, 2049–2059.

(31) Zhu, Y.; Zhang, J.; Meng, F.; Deng, C.; Cheng, R.; Feijen, J.; Zhong, Z. cRGD/TAT dual-ligand reversibly cross-linked micelles loaded with docetaxel penetrate deeply into tumor tissue and show high antitumor efficacy in vivo. *ACS Appl. Mater. Interfaces* **2017**, *9*, 35651–35663.

(32) Li, Y.; Wei, J.; Wei, Y.; Cheng, L.; Guo, B.; Meng, F.; Li, F.; Zhong, Z. Apolipoprotein E peptide-guided disulfide-cross-linked micelles for targeted delivery of sorafenib to hepatocellular carcinoma. *Biomacromolecules* **2020**, *21*, 716–724.

(33) Zou, Y.; Fang, Y.; Meng, H.; Meng, F.; Deng, C.; Zhang, J.; Zhong, Z. Self-crosslinkable and intracellularly decrosslinkable biodegradable micellar nanoparticles: A robust, simple and multifunctional nanoplatform for high-efficiency targeted cancer chemotherapy. *J. Controlled Release* **2016**, *244*, 326–335.

(34) Fang, Y.; Jiang, Y.; Zou, Y.; Meng, F.; Zhang, J.; Deng, C.; Sun, H.; Zhong, Z. Targeted glioma chemotherapy by cyclic RGD peptide-functionalized reversibly core-crosslinked multifunctional poly(ethylene glycol)-b-poly(epsilon-caprolactone) micelles. *Acta Biomater.* **2017**, *50*, 396–406.

(35) Wei, J.; Meng, H.; Guo, B.; Zhong, Z.; Meng, F. Organocatalytic ring-opening copolymerization of trimethylene carbonate and dithiolane trimethylene carbonate: Impact of organocatalysts on copolymerization kinetics and copolymer microstructures. *Biomacromolecules* **2018**, *19*, 2294–2301.

(36) Ding, L.; Gu, W.; Zhang, Y.; Yue, S.; Sun, H.; Cornelissen, J. J. L. M.; Zhong, Z. HER2-specific reduction-sensitive immunopoly-mersomes with high loading of epirubicin for targeted treatment of ovarian tumor. *Biomacromolecules* **2019**, *20*, 3855–3863.

(37) Banks, W. A. From blood–brain barrier to blood–brain interface: new opportunities for CNS drug delivery. *Nat. Rev. Drug Discovery* **2016**, *15*, 275–292.

(38) Qin, H.; Jiang, Y.; Zhang, J.; Deng, C.; Zhong, Z. Oncoprotein inhibitor rigosertib loaded in ApoE-targeted smart polymersomes reveals high safety and potency against human glioblastoma in mice. *Mol. Pharm.* **2019**, *16*, 3711–3719.

(39) Qian, W.; Qian, M.; Wang, Y.; Huang, J.; Chen, J.; Ni, L.; Huang, Q.; Liu, Q.; Gong, P.; Hou, S.; Zhu, H.; Jia, Z.; Shen, D.; Zhu, C.; Jiang, R.; Sun, J.; Yao, J.; Tang, Z.; Ji, X.; Shi, J.; Huang, R.; Shi, W. Combination glioma therapy mediated by a dual-targeted delivery system constructed using OMCN-PEG-Pep22/DOX. *Small* **2018**, *14*, 1801905.

(40) Kim, J. S.; Choi, G. H.; Jung, Y.; Kim, K. M.; Jang, S.-J.; Yu, E. S.; Lee, H. C. Downregulation of Raf-1 kinase inhibitory protein as a sorafenib resistance mechanism in hepatocellular carcinoma cell lines. *J. Cancer Res. Clin. Oncol.* **2018**, *144*, 1487–1501.

(41) Wang, J.-L.; Du, X.-J.; Yang, J.-X.; Shen, S.; Li, H.-J.; Luo, Y.-L.; Iqbal, S.; Xu, C.-F.; Ye, X.-D.; Cao, J.; Wang, J. The effect of surface poly(ethylene glycol) length on in vivo drug delivery behaviors of polymeric nanoparticles. *Biomaterials* **2018**, *182*, 104–113.

(42) Chen, M.-L.; Yan, B.-S.; Lu, W.-C.; Chen, M.-H.; Yu, S.-L.; Yang, P.-C.; Cheng, A.-L. Sorafenib relieves cell-intrinsic and cell-extrinsic inhibitions of effector T cells in tumor microenvironment to augment antitumor immunity. *Int. J. Cancer* **2014**, *134*, 319–331.

(43) Sheng, Z.; Li, L.; Zhu, L. J.; Smith, T. W.; Demers, A.; Ross, A. H.; Moser, R. P.; Green, M. R. A genome-wide RNA interference screen reveals an essential CREB3L2-ATF5-MCL1 survival pathway in malignant glioma with therapeutic implications. *Nat. Med.* **2010**, *16*, 671–677.